Journal of *Marine Science and Engineering*

MDPI

Article

Numerical Analysis of Water-Injection Drag Reduction on a Flat Plate

David Hitchmough [1,*], Anas Muhamad Pauzi [1], Eddie Blanco-Davis [1,*], Andrew Spiteri [1], Ava Shahrokhi [1], Alex Routledge [2], Roger Armson [2], Nikolaos Tsoulakos [3] and Jin Wang [1]

[1] Liverpool Logistics, Offshore and Marine Research Institute (LOOM), School of Engineering, Liverpool John Moores University, Byrom Street, Liverpool L3 3AF, UK
[2] Armada Technologies, Rodney Chambers, 40 Rodney Street, Liverpool L1 9AA, UK
[3] Laskaridis Shipping Co., Ltd., 5 Xenias Str. & Ch. Trikoupi, 14562 Athens, Greece
* Correspondence: d.m.hitchmough@ljmu.ac.uk (D.H.); e.e.blancodavis@ljmu.ac.uk (E.B.-D.)

Abstract

Water injection is a promising alternative to traditional air lubrication for reducing ship hull drag and improving energy efficiency. Addressing the limited research on the efficacy of water lubrication on ships, this novel study is the first to numerically evaluate its performance on a flat-plate model, systematically investigating key operational and geometrical parameters. The rectangular flat plate model of finite thickness represents a 1:56 scale of the Japan Bulk Carrier hull. The study conducts Reynolds-Averaged Navier–Stokes (RANS) simulations using the commercial CFD package STAR-CCM+ and systematically investigates the effects of injection angle, velocity ratio, flow rate, Reynolds number, and plate orientation. The results indicate that an injection angle of 60–90° is optimal, with an ideal velocity ratio (U_{Inj}/U_b) of approximately 1.5, resulting in a drag reduction of up to 38.8%. The flow-rate ratio (Q_{Inj}/Q_w) also serves as a pertinent scaling parameter, with an optimum at 1.1. The study found that the primary drag reduction mechanism is the decrease in skin friction, which, unlike pressure-driven effects, is robust across different plate orientations. These findings underscore the potential of water injection as a scalable and effective strategy for maritime decarbonisation, exhibiting performance that is robust and stable across a wide range of Reynolds numbers and plate orientations.

Keywords: water lubrication; Computational Fluid Dynamics (CFD); drag reduction; decarbonisation; ship resistance

Academic Editors: Md Jahir Rizvi and Decheng Wan

Received: 13 October 2025
Revised: 20 November 2025
Accepted: 25 November 2025
Published: 28 November 2025

Citation: Hitchmough, D.; Muhamad Pauzi, A.; Blanco-Davis, E.; Spiteri, A.; Shahrokhi, A.; Routledge, A.; Armson, R.; Tsoulakos, N.; Wang, J. Numerical Analysis of Water-Injection Drag Reduction on a Flat Plate. *J. Mar. Sci. Eng.* **2025**, *13*, 2271. https://doi.org/10.3390/jmse13122271

1. Introduction and Existing Literature

Reducing skin friction is a crucial pathway for enhancing energy efficiency and achieving international decarbonization targets. Improving hull efficiency not only reduces fuel consumption and operating costs but also contributes directly to emissions reduction, making drag-reduction technologies a high priority in maritime research.

A wide range of strategies has been developed to mitigate skin-friction drag. Conventional approaches include hull form optimisation, antifouling coatings, and passive surface modifications such as riblets or biomimetic textures [1]. More advanced techniques employ active boundary-layer control, with air lubrication being the most extensively studied. Air lubrication, introduced as early as the 1960s [2], injects bubbles or forms air sheets beneath the hull to reduce the wetted area and modify fluid properties near the wall. Reported drag-reduction levels range from less than 5% [3] to as high as 80% under

controlled conditions [4]. In full-scale practice, however, net savings typically remain in the 5–10% range. Although widely trialled, air lubrication still faces challenges with bubble stability, energy costs, and reduced effectiveness on deep-draft or side-wall surfaces.

Beyond passive and multiphase methods, jet injection has shown promise in actively manipulating boundary-layer dynamics for drag reduction. Studies across aerospace, hydrodynamics, and bluff-body flows demonstrate that jets can recover velocity gradients, suppress turbulence, and alter near-wall shear stresses. For example, pulsed and tangential jets directed along curved rear surfaces (via the Coandă effect) kept the flow attached, reduced the wake size, and raised wake pressure, achieving drag reductions of up to 20% [5]. In underwater applications, Computational Fluid Dynamics (CFD) investigations on axisymmetric vehicles confirmed that jet angle and momentum ratio strongly influence resistance reduction, with stern geometry playing a key role, as the shape of the stern dictates the nature of flow separation and the size of the wake, which the jet injection is intended to manipulate [6]. Synthetic jet injection has also been explored in combination with modern optimisation methods. The authors of [7] applied multi-agent reinforcement learning to coordinate arrays of synthetic jets on a turbulent cylinder, achieving an 8% reduction with far greater efficiency than classical actuation methods. The findings of [7] highlight that the outcome of jet injection depends strongly on the injection angle and the jet-to-freestream momentum ratio. When these parameters are selected correctly, jets can produce a weaker, more stable flow separation that lowers near-wall stresses and contributes to drag reduction. In contrast, unsuitable parameter choices can intensify turbulent mixing and raise drag instead of reducing it [6,8,9]. For marine applications, this implies that carefully positioned slot-jet systems on ship hulls could provide robust drag reduction, particularly at greater depths and on side walls. However, scaling up to full-size vessels will require careful balancing of injection energy costs against performance gains, supported by systematic CFD and experimental studies.

Compared to air lubrication, water lubrication is a relatively underexplored concept. Rather than introducing air—a dissimilar, less dense, and less viscous gaseous phase—water injection utilises the same fluid medium as the bulk flow to modify the boundary layer actively. This distinction is critical because it avoids the limitations of bubble entrainment, stability, and buoyancy effects that plague air lubrication, especially at greater depths or on inclined surfaces. Specifically, water injection reduces drag primarily through modification of skin friction, suggesting applicability across different plate orientations. This offers potential applicability across a wider range of hull geometries, including side walls and deep-draft sections, where air lubrication is less effective. Recent studies suggest two primary mechanisms: (i) controlled induction of flow separation to create a slowly moving or reverse-flowing layer near the wall, thereby reducing shear stress [10] and (ii) modification of velocity gradients to form a low-shear boundary layer [11]. Although flow separation is typically associated with increased drag, these findings demonstrate that, if carefully induced, it can be exploited to reduce wall shear instead. This inversion of a traditionally adverse phenomenon represents a novel direction in hull drag reduction.

It is crucial to distinguish these water injection techniques for drag reduction from air lubrication methods. Air lubrication typically involves the injection of air bubbles or the creation of an air layer beneath the hull to reduce the contact area between the hull and the water or to alter the fluid properties within the boundary layer by introducing a less dense and viscous medium. In contrast, water injection focuses on manipulating the hydrodynamic flow of water within the boundary layer to achieve drag reduction, without introducing a gaseous phase for lubrication purposes. The basis of air lubrication has been established much more firmly than that of water lubrication. Research on air lubrication has been ongoing, with varying levels of interest and intensity since at least

the 1970s. Some early research was carried out at the Krylov Shipbuilding Institute in the 1960s, as discussed in the work of [2]. Due to the more extensive basis of work on air lubrication, we have a better understanding of the principle and working mechanism in this case, as well as the potential drag-reducing effect. The drag-reducing effect results from the air modifying the wetted surface area, viscosity, wall shear and hence turbulence. However, the exact physics and causes of the drag-reducing effect remain a matter of debate [12]. The level of drag reduction achieved through air lubrication is highly variable, depending on the operating conditions and the geometry, particularly when comparing flat plate test conditions to real-world testing data. Some studies have shown drag reduction levels of below 5% [3], whereas others have demonstrated reductions of as much as 80% in skin frictional drag [4]. In real-world conditions, air lubrication can typically achieve a net saving of 5 to 10%. The application of water lubrication remains at a low technology readiness level, and systematic studies under ship-relevant conditions are lacking. The present project, therefore, aims to develop a computational framework for water lubrication, combining CFD simulations with parametric analyses of injection rate, angle, and Froude number. By benchmarking against established wall lubrication methods, this work aims to develop a physical understanding of water-jet-induced boundary layer modification and assess its potential as a robust and scalable drag reduction strategy for future ship designs.

Recent studies highlight several active drag-reduction mechanisms. Polymer and bio-polymer injections, such as polyethylene oxide [13] and yam mucilage [14], achieve drag reduction through viscoelastic effects, where stretched molecular chains increase extensional viscosity and dampen near-wall turbulence. Similarly [15] uses a method of slow release polymer to achieve drag reduction, which has some similarities to the use of water lubrication; however in contrast, the present study investigates a single-phase water-injection approach, which is expected to reduce drag primarily through hydrodynamic modification of the near-wall shear rather than changes in turbulence structure.

There is currently limited direct research on water lubrication technology. In some respects, air lubrication provides a precedent for the principles involved in water lubrication. However, the lubrication vector is fundamentally different between the two technologies, with air lubrication using a non-like fluid to lubricate the ship's hull, thereby preventing contact with the water. Water injection for drag reduction on ships involves the intentional introduction of water into the boundary layer, the thin layer of fluid directly adjacent to the hull surface. The fundamental principle behind this approach is to manipulate the flow characteristics within this boundary layer in a way that reduces the frictional forces between the water and the hull. Unlike air lubrication, which introduces air with significantly lower viscosity into the boundary layer, water injection utilises the same fluid medium as the bulk flow.

The primary mechanisms through which water injection can lead to drag reduction are related to the controlled alteration of the boundary layer. One proposed mechanism in [10] involves the use of water jets to induce a localised separation of the flow from the hull surface. When implemented correctly, this separation can create a thin layer of slowly moving or even reverse-flowing fluid near the wall, effectively reducing the shear stress and hence the frictional drag. This concept could be seen as counterintuitive, as separation is generally associated with increased drag due to the formation of a wake. However, in the case of a flat plate, carefully positioned separations can lead to the formation of a sluggish boundary layer that minimises drag. Another potential mechanism involves the creation of a low-shear layer through the interaction of injected water with the existing boundary layer flow. By precisely controlling the velocity and direction of the injected water, it may be possible to modify the velocity gradient near the hull, leading to a reduction in skin friction [11].

Following this section, the remainder of the paper is structured as follows: Section 2 details the Computational Fluid Dynamics (CFD) methodology, including the geometry, fluid properties, and numerical setup. Section 3 presents the verification and validation studies, which cover mesh and time-step independence, as well as benchmarking against analytical correlations. Section 4 discusses the parametric investigation into injection angle, scaling parameters, and the underlying flow mechanisms. Section 5 examines the impact of plate orientation, and Section 6 concludes the study with a summary of the key findings and recommendations for future research.

2. Simulation Methodology

The water-injection drag reduction was investigated using Reynolds-Averaged Navier–Stokes (RANS) simulations. All computations were performed using the commercial Computational Fluid Dynamics (CFD) package STAR-CCM+ (Version 2021.1). The transient RANS approach was employed to capture the evolution of turbulent vortices and the mixing effects resulting from water injection. Turbulence was modelled using the k–ω SST formulation, chosen for its robustness in accurately predicting near-wall shear and separating flows, which is critical for fluid lubrication studies. Since both the freestream and injected flows consist of the same fluid (water), a single-phase Volume of Fluid (VOF) formulation was employed, which avoids unnecessary interface tracking and allows the natural mixing to be resolved directly by the turbulence model.

2.1. Geometry and Fluid Properties

Details of the fluid and geometrical properties of the simulation domain are presented in Table 1, and a schematic diagram of the setup is shown in Figure 1.

Table 1. Fluid and geometry properties.

Properties	Values
Fluid (Water)	
Density, ρ [kg/m^3]	997.561
Kinematic viscosity, ν [m^2/s]	8.90883×10^{-7}
Freestream velocity, U [m/s]	0.3–1.5
Reynolds number on the plate, Re_L ($\times 10^6$)	1.68–8.42
Injection velocity, U_{inj} [m/s]	0.1–3.0
Geometry	
Tank	
-Length, L_{Tank} [m]	30
-Width. B_{Tank} [m]	8
-Height. T_{Tank} [m]	8
Flat plate	
-Length, L [m]	5
-Width, B_{WL} [m]	0.804
-Height, T [m]	0.295
Injection slot	
-Length, L_{inj} [m]	0.05
-Width, B_{inj} [m]	0.78
-Angle, θ_{Inj} [°]	15–90

As shown in Figure 1, the flat plate is centrally positioned in the tank, with an upstream length of 10 m and a downstream length of 15 m. Although described here as a flat plate, the model has a finite thickness (T = 0.295 m) to ensure structural strength and realistic boundary-layer development in a three-dimensional domain. The analysis focuses on the lower surface, which behaves as a locally flat wall. This geometry is also practical for future experimental validation, as a plate of finite thickness can be built and tested using the same

dimensions and injection setup. The injection slot located 0.1 m (2% L) downstream from near the leading edge on the bot-tom surface of the plate. This position was selected to allow the water injection to interact with the developing boundary layer near the transition region while avoiding the stagnation point at the leading edge. The slot spans, has a span of 0.78 m, corresponding to 97% of the plate width. All other tank boundaries are treated as no-slip walls, while the inlet and outlet are defined by fixed value velocity and zero gradient pressure outlet conditions, respectively. Gravity was enabled in all simulations, acting in the global -y direction, to reproduce the hydrostatic pressure field in water.

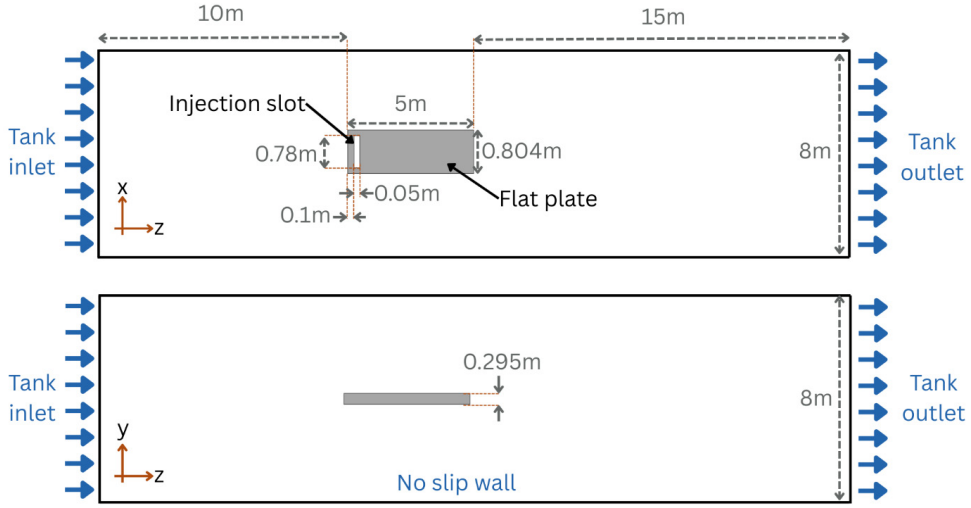

Figure 1. Schematic diagram of simulation domain (not to scale).

2.2. Numerical Method and Mesh Setup

The baseline simulation was performed at a mid-range Reynolds number of 5.61×10^6 (corresponding to a free-stream velocity of 1 m/s or ~1.94 knots), with water injected at twice the free-stream velocity ($U_{Inj}/U_b = 2$) and at 90° to the bottom surface near the upstream end of the plate.

Turbulence was modelled using the k–ω SST formulation, which is widely applied in fluid lubrication studies due to its robustness in predicting near-wall shear and separating flows [16,17]. STAR CCM+'s "All y^+ wall treatment" option was utilised, which is a blended option between the High and Low y^+ options; therefore, by ensuring a non-dimensional wall distance of $y^+ < 5$ across the entire plate surface (Figure 2), the model wall treatment approach functions as the Low y^+ option [18]. Although the strict low-y^+ formulation generally targets y^+ around unity, the "All y^+ treatment" reproduces this low-Re behaviour for fine meshes ($y^+ \leq 5$) while maintaining solver stability at large Reynolds numbers [15]. Similar y^+ targets are also commonly adopted in wall-resolved marine CFD studies [19,20], supporting the suitability of this resolution for drag-prediction. The selection of the All y^+ option provides both wall-resolved accuracy and robustness when local y^+ variation occur.

The simulations employed a transient RANS approach to capture the evolution of turbulent vortices and the mixing effects induced by water injection. Although the injected and freestream flows have different velocities, both consist of the same fluid (water). Therefore, a single-phase Volume of Fluid (VOF) formulation is adopted rather than a multi-phase VOF method. Avoiding a multiphase-like treatment in this context is advantageous, as it removes unnecessary interface tracking and allows the natural mixing between the injected and bulk flows to be resolved directly by the turbulence model.

The mesh characteristics utilised for the work are summarised in Table 2, while the numerical schemes and solver settings are given in Table 3. Representative mesh views at selected cross-sections are presented in Figure 3. All computations were performed

using Siemens STAR-CCM+ v16.02.009-R8 [18]. Parallel execution was carried out on 64 CPU cores within a single compute node of Liverpool John Moores University's high-performance computing cluster, Prospero [21].

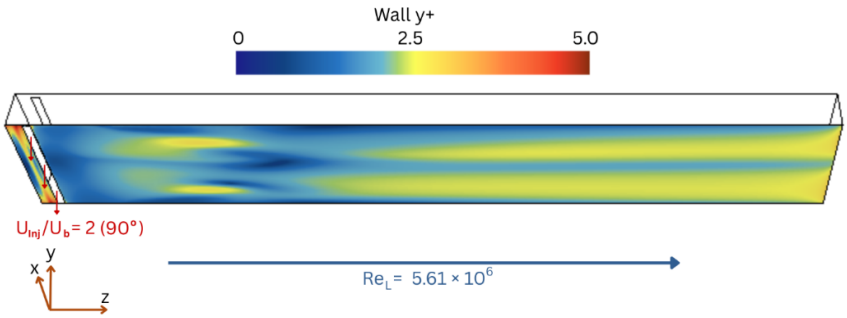

Figure 2. Contours of dimensionless near-wall distance, y^+, on the flat plate for the baseline simulation ($Re_L = 5.61 \times 10^6$, $U_{Inj}/U_b = 2$, $\theta_{Inj} = 90°$). The computational axes are shown for reference, with "x" aligned spanwise, "y" wall-normal, and "z" streamwise.

Table 2. Meshing Settings influenced by [22].

Parameter	Values
Mesh type	Trimmed hexahedral cells with a prism layer
Base size	0.256 m
Prism layers	28 layers, first layer thickness $y^+ < 5$, stretching ratio 1.2
Refinement regions	Around the flat plate, near the injection region and near the plate bottom
Surface size near the plate	7.5% relative to base size
Surface size near the injection slot	5.0% relative to base size
Surface size near the plate bottom	2.5% relative to base size
Total cell count	6.13–6.4 million (depending on injection angle)
Minimum surface quality	0.05

Note: The mesh was verified through a mesh-independence study in Section 3.

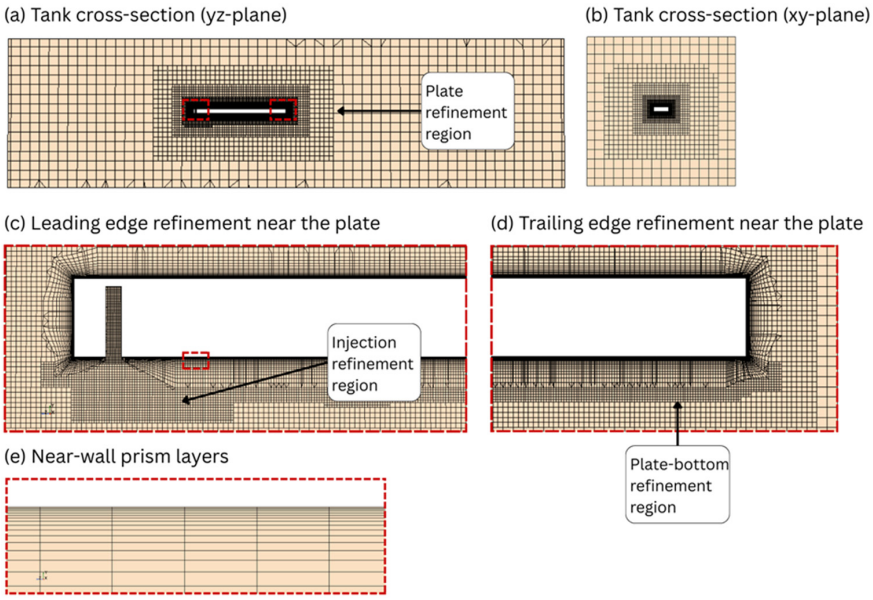

Figure 3. Representative mesh distribution at selected locations: (**a**) tank cross-section in the yz-plane; (**b**) tank cross-section in the xy-plane; (**c**) near the leading edge of the plate; (**d**) near the trailing edge; and (**e**) near-wall prism layers.

Table 3. Numerical schemes and solver settings according to [18].

Parameter	Schemes/Settings
Pressure-velocity coupling	SIMPLE algorithm with Rhie-Chow interpolation
Temporal discretisation	Second-order implicit backwards scheme, fixed time step size, Δt and 10 inner iterations per time step.
Spatial discretisation (convection)	Second-order upwind
Solver type	Segregated (equations solved sequentially, re-coupled through pressure correction)
Linear solvers	Algebraic Multigrid (AMG)
Gradient schemes	Least-squares with Venkatakrishnan limiter

3. Verification and Validation

3.1. Sensitivity Studies

Resolution verification was conducted in accordance with the ITTC's recommended procedures [23]. The drag force on the plate surface was monitored until oscillatory convergence was achieved, which occurred approximately 60 s into the simulated time (Figure 4a). For non-monotonic convergence behaviour, numerical uncertainty was quantified using the least-squares-fit method of [24], which is particularly suited for oscillatory or irregular convergence trends. Both time-step and mesh-size independence studies were performed using four refinement levels. The corresponding results are summarised in Tables 4 and 5, and the trends are illustrated in Figure 4b,c.

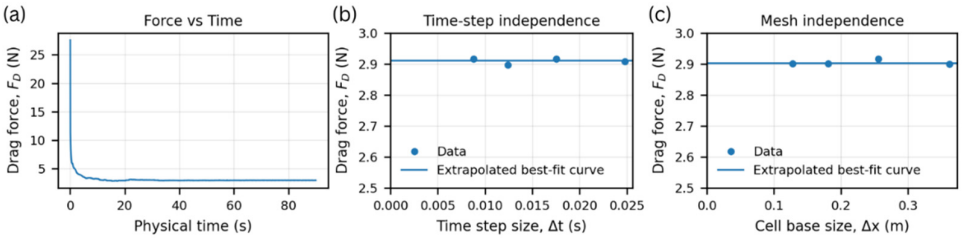

Figure 4. Resolution verification of drag force: (**a**) convergence of drag force with simulation time, (**b**) time-step independence study, and (**c**) mesh independence study.

Table 4. Time-step independence study.

Level	Time Step Size, Δt (s)	Drag Force, F_D (N)	Best Fit Curve, F_{Fit} (N)	Relative Uncertainty, ε_F/F (%)
Coarse	0.02481	2.908	2.9106	0.6%
Medium	0.01754	2.917	2.9106	0.7%
Fine	0.0124	2.897	2.9106	0.9%
Finest	0.00877	2.917	2.9106	0.6%

Table 5. Mesh independence study.

Level	Base Cell Size, Δx (m)	Number of cells ($\times 10^6$)	Drag Force, F_D (N)	Best Fit Curve, F_{Fit} (N)	Relative Uncertainty, ε_F/F (%)
Coarse	0.362	2.67	2.9	2.9040	0.9%
Medium	0.256	6.13	2.917	2.9034	1.0%
Fine	0.181	11.13	2.901	2.9032	0.6%
Finest	0.128	25.5	2.901	2.9031	0.5%

Both studies yielded an estimated numerical uncertainty of less than 1%, providing strong evidence for the adequacy of the chosen resolution. Accordingly, a medium mesh

and a medium time step were used for all subsequent simulations to strike a balance between accuracy and computational efficiency.

3.2. Validation of Flat-Plate Correlations

To evaluate the accuracy of the k–ω SST simulations, the predicted skin frictional drag coefficients of a smooth flat plate were benchmarked against classical analytical and empirical correlations for zero-pressure-gradient boundary layers. The Blasius laminar solution represents the theoretical lower limit of C_f. In contrast, the ITTC-1957 correlation [25] and the Prandtl–Schlichting 1/5th power law [26] provide upper bounds corresponding to a fully turbulent boundary layer from the leading edge.

As illustrated in Figure 5, the CFD results consistently fall between the laminar and turbulent limits across the examined Reynolds number range, in line with expectations for a transitional boundary layer [27]. At lower Reynolds numbers, the predictions are closer to the laminar solution, while at higher Reynolds numbers, they tend towards the turbulent correlations. This bounded behaviour indicates that the k–ω SST model reproduces the correct physical trend. To further benchmark the results, a fully turbulent smooth-wall data point was reconstructed from the literature [28] at $Re_L = 4.9 \times 10^6$ was added to Figure 5. Although the precise onset of laminar-to-turbulent transition is not explicitly prescribed, the predicted skin frictional drag coefficients lie below the fully turbulent experimental value, as expected for an untripped and partially transitional plate, but remain within accepted theoretical limits, thereby increasing confidence in the reliability of the present simulations.

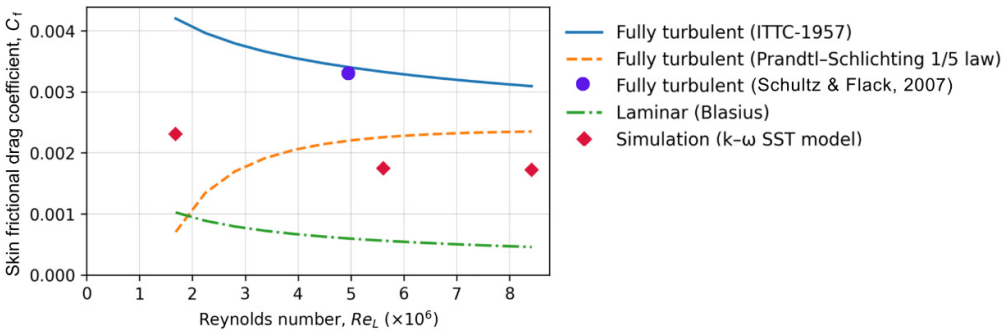

Figure 5. Comparison of CFD results, analytical and empirical correlations, and experiment data for the flat plate skin frictional coefficient [25,26,28].

4. Parametric Investigation

4.1. Definition of Parameters

A dimensional analysis based on the Buckingham Pi theorem [29] (see Appendix A) identified two independent non-dimensional parameters:

Injection velocity ratio, U_{Inj}/U_b
Injection flow rate ratio, Q_{Inj}/Q_w

Here, Q_{Inj} is the volumetric injection rate, determined from the injection velocity and the cross-sectional area of the injection slot ($Q_{Inj} = U_{Inj}A_{Inj}$). The wall flow rate Q_w represents the volumetric flow within the boundary layer and is estimated using the empirical correlation (1) presented by [30], which is derived from the Prandtl–Schlichting 1/5th power law [26].

$$Q_w = 0.293 L^{0.8} \nu^{0.2} U_b^{0.2} B \quad (1)$$

where L and B are the length and width of the flat plate, ν is the kinematic viscosity, and U_b is the bulk velocity.

The velocity ratio, U_{Inj}/U_b, represents the relation between the injected velocity and the freestream (global) velocity, while the flow-rate ratio, Q_{Inj}/Q_w, accounts for the combined effects of momentum and volumetric flux within the boundary layer.

Drag reduction (DR) was evaluated by comparing the skin frictional drag force on the plate bottom surface with and without water injection, as defined in (2).

$$\mathrm{DR}(\%) = \frac{\mathrm{F_D} - \mathrm{F_{D0}}}{\mathrm{F_{D0}}} \times 100 \tag{2}$$

where F_D represents the skin frictional drag force with injection, and F_{D0} represents the skin frictional drag force without injection.

For reference, the skin frictional coefficient, C_f, is defined as shown in (3).

$$\mathrm{C_f} = \frac{\tau_\mathrm{w}}{0.5\rho \mathrm{U_b^2}} \tag{3}$$

where τ_w is the wall shear stress, ρ is the density of water, and U_b is the bulk velocity.

4.2. Effect of Injection Angle

Research on the role of injection angle in water jet drag reduction remains limited. Perpendicular (90°) injection has been examined in earlier work [10], while more recent studies have explored angles from 90° down to 30°, showing that angle variation can influence drag reduction performance [11].

In the present study, the injection angle was varied from 90° (normal to the surface) to 15° in the downstream direction, under the same operating conditions. (U_b = 1.0 m/s, $\mathrm{Re_L} = 5.61 \times 10^6$, U_{Inj}/U_b = 2.0). The slot-present, non-injection case (Figure 6a) serves as the reference for quantifying drag reduction at each angle. A summary of the drag values achieved for the different injection angles, along with the corresponding percentage drag reductions relative to the baseline, is provided in Table A3 in Appendix B.

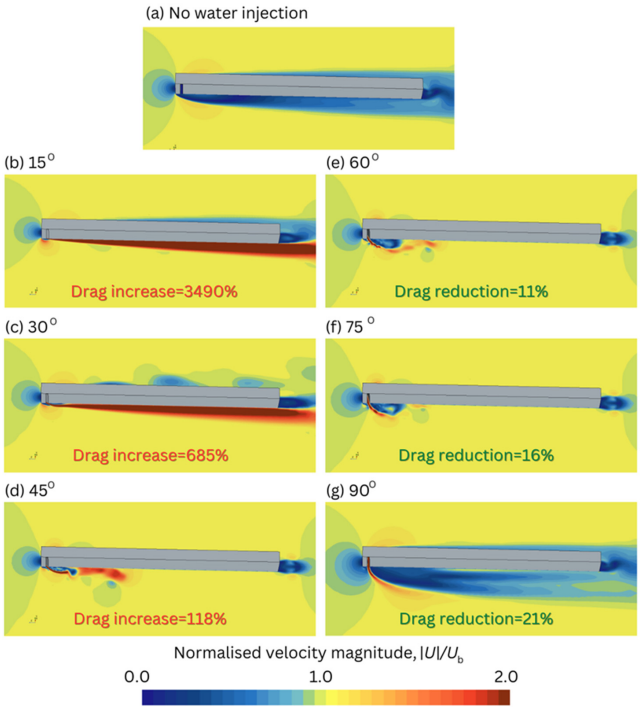

Figure 6. Contours of normalised velocity magnitude ($|U|/U_\mathrm{b}$) at the plate bottom for (**a**) the slot-present non-injection baseline, and for injection angles, θ_Inj: (**b**) 15°, (**c**) 30°, (**d**) 45°, (**e**) 60°, (**f**) 75°, and (**g**) 90° for the baseline simulation ($\mathrm{Re_L} = 5.61 \times 10^6$, $U_\mathrm{Inj}/U_\mathrm{b}$ = 2).

Results showed a continuous decline in drag reduction as the injection angle decreased. While larger angles (60–90°) produced a positive drag reduction of 10–20%, smaller angles resulted in an apparent drag increase, which warrants further investigation in future studies. Considerable increases were observed at 15° and 30° as illustrated in Figure 6. At larger angles, the injection of water induces flow separation in the region under the plate and areas of recirculation near the wall, which correspond to areas of reduced skin friction. In contrast, at smaller angles, the jet is directed more along the plate surface, accelerating the near-wall flow, which may explain the considerable increase in the overall drag force. The finding that the highest level of drag reduction occurs at a 90° angle agrees with the approach of [10], while drag reduction across a broader range from 90° down to 30° has also been reported [11]. Based on these findings, the subsequent simulations will focus on injection angles between 60° and 90°, as this range has consistently demonstrated positive drag reduction effects.

4.3. Scaling Parameters: Velocity Ratio vs. Flow-Rate Ratio

The effectiveness of injection scaling was first examined using both the injection flow-rate ratio (Q_{Inj}/Q_w) and the injection velocity ratio (U_{Inj}/U_b). Figure 7 compares the drag-reduction trends for bulk velocities of U_b = 1.0 and 1.5 m/s expressed in terms of each parameter. The corresponding numerical values are given in Table A4 in Appendix B.

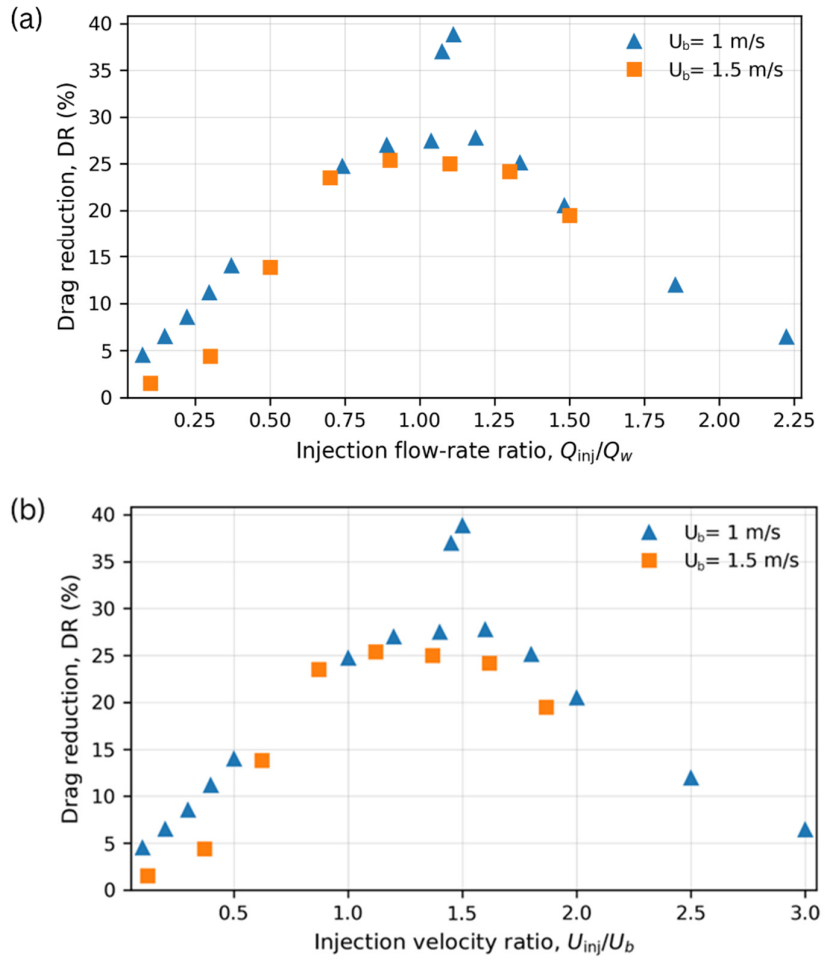

Figure 7. Effect of injection ratio scaling on drag reduction for bulk velocities of U_b = 1 m/s and U_b = 1.5 m/s: (**a**) Injection flow rate ratio, Q_{Inj}/Q_w, and (**b**) injection velocity ratio, U_{Inj}/U_b.

Both ratios produce similar shapes, with drag reduction reaching a peak near the optimum and then declining at higher values. The overall similarity reflects the fact that at

constant Reynolds number and aspect ratio, the two parameters are directly proportional (Equation (A1) in Appendix A). However, for both injection ratios in Figure 7, the drag reduction at U_b = 1.5 m/s is consistently lower than at U_b = 1.0 m/s, reflecting the weaker influence of injection momentum at higher freestream bulk velocity. A closer comparison reveals that the velocity-ratio scaling (Figure 7b) collapses the data more effectively, particularly around the optimum, whereas the flow-rate ratio (Figure 7a) introduces additional scatter due to its sensitivity to Reynolds number through the estimation of Q_w.

To further examine this behaviour, Figure 8 compares the drag reduction at U_b = 1.0 m/s for the optimum injection flow-rate ratio (Q_{Inj}/Q_w = 1.1, from Figure 7a) and the optimum injection velocity ratio (U_{Inj}/U_b = 1.5, from Figure 7b) across different Reynolds numbers. The corresponding values are tabulated in Table A5 in Appendix B.

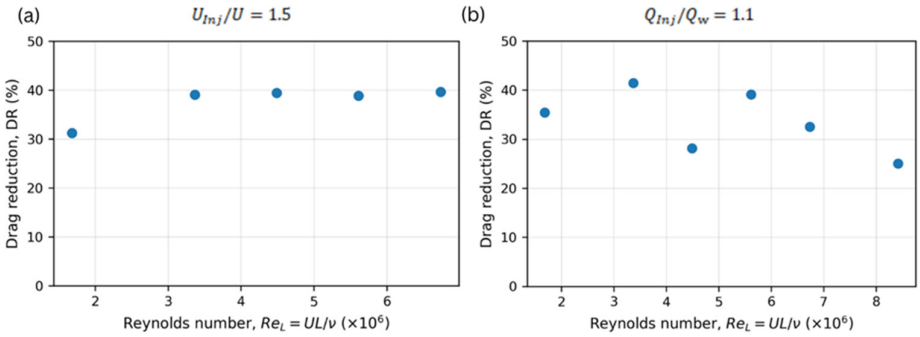

Figure 8. Drag reduction as a function of Reynolds number, Re_L, at a fixed non-dimensional injection parameter: (**a**) injection velocity ratio, U_{Inj}/U_b = 1.5, and (**b**) injection flow rate ratio, Q_{Inj}/Q_w = 1.1.

Figure 8a shows that when the injection velocity ratio is fixed at U_{Inj}/U_b = 1.5, the drag reduction remains consistently high, between 30% and 40%. As the Reynolds number increases from 1.68 × 10^6, the drag reduction rises and stabilises within the range 3.37 × 10^6 to 6.73 × 10^6, suggesting that this velocity ratio is practical and applicable across this operating regime, which is representative of the JBC reference condition. The variation of Re_L also influences the reference water injection flow rate, Q_w (refer to Equation (1)), since both quantities depend on the bulk velocity, U_b ($Re_L = U_bL/\nu$). Because the viscosity (ν) variation is set constant across the cases, the trend in Figure 8a primarily reflects the effect of increasing U_b, rather than changes in fluid properties.

In contrast, Figure 8b demonstrates that at the optimum injection flow-rate ratio of Q_{Inj}/Q_w = 1.1, the drag reduction varies more widely, between 25% and 42%. The values are more scattered, with a dip at mid-range Reynolds numbers around 4.5 × 10^6, followed by a gradual decline to a minimum at the highest Reynolds number tested (8.42 × 10^6). This indicates that, although useful, the flow-rate ratio (Q_{Inj}/Q_w) is less robust than the velocity ratio (U_{Inj}/U_b) as a scaling parameter for predicting drag-reduction performance. Accordingly, U_{Inj}/U_b is adopted as the primary scaling parameter in the following analysis.

4.4. Effect of Injection at Fixed Bulk Velocity

To better understand the mechanisms underlying drag reduction, the flow fields were examined at a fixed bulk velocity of U_b = 1.0 m/s across a range of injection velocity ratios.

Figure 9 presents contours of normalised streamwise velocity and the corresponding skin-friction coefficient for selected cases. Without injection (Figure 9a), a small degree of separation occurs at the leading edge and reattaches around mid-chord. Downstream of reattachment, the skin-friction field becomes spanwise uniform and symmetric, with a well-defined low-friction region along the centreline.

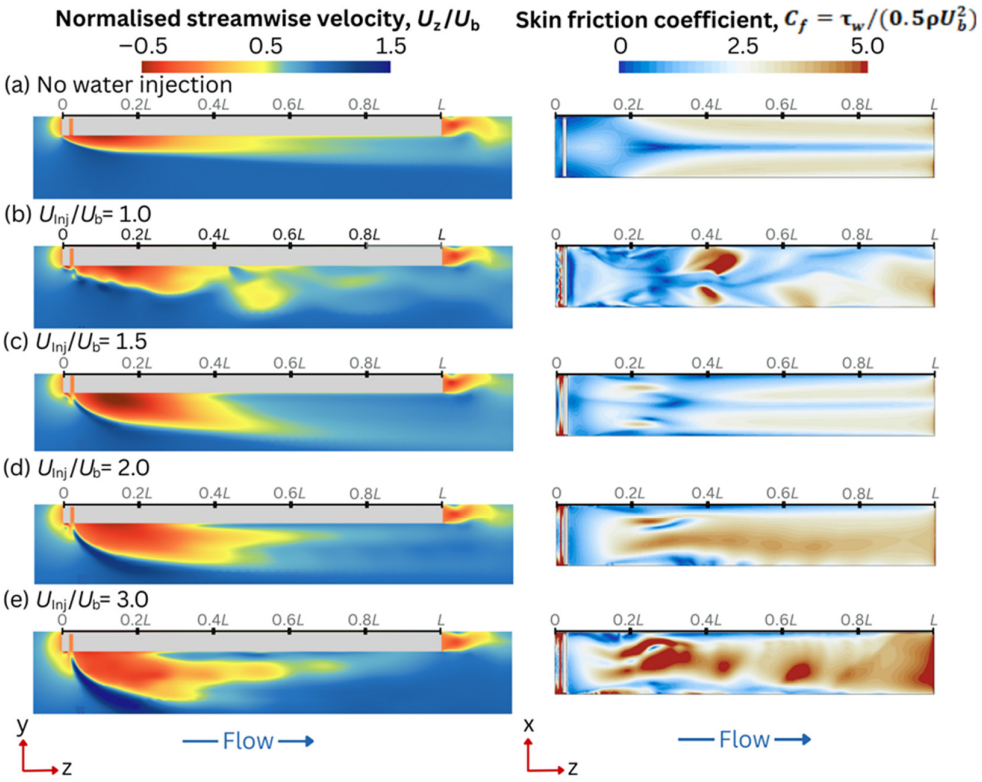

Figure 9. Contours of (**left**) normalised streamwise velocity, U_Z/U_b and (**right**) skin friction coefficient, C_f at selected injection velocity ratios: (**a**) No water injection, (**b**) U_{Inj}/U_b = 1.0, (**c**) U_{Inj}/U_b = 1.5, (**d**) U_{Inj}/U_b = 2.0 and (**e**) U_{Inj}/U_b = 3.0.

With an injection ratio of U_{Inj}/U_b equal to 1.0 (Figure 9b), the interaction between the injected jet and the leading-edge separation induces a stronger interaction between the injected and freestream flow. The reattachment point moves upstream, while zones of low streamwise velocity are displaced away from the wall. The corresponding skin-friction plot shows spanwise asymmetry, with the low-friction core displaced laterally and a strong localised peak near x/L ≈ 0.4 marking an intense reattachment.

According to Figure 7, the optimum ratio of U_{Inj}/U_b is 1.5. This is where the maximum level of drag reduction is achieved (Figure 9c). The separated region enlarges but exhibits weaker skin-friction peaks at reattachment. The skin-friction field recovers a more symmetric distribution, with the lowest-friction region returning closer to the centreline, although not as dominant as in the no-injection case.

Increasing the ratio to U_{Inj}/U_b to 2.0 (Figure 9d), reattachment occurs earlier, although the area of recirculation remains in proximity to the wall for a greater distance downstream, with reduced backflow intensity compared with U_{Inj}/U_b = 1.5.

The skin-friction distribution again becomes asymmetric, and the low-friction centreline band is no longer evident. At the highest ratio of U_{Inj}/U_b = 3.0 (Figure 9e), reattachment occurs very close to the leading edge (around x/L ≈ 0.25). Small-scale alternating zones of high and low skin friction develop downstream, with the lowest friction regions shifted toward the sides of the plate. Overall, the skin-friction levels are higher than in the no-injection case, despite localised low-friction patches.

To further capture the behaviour of the injected water, a streamline scene was created, as shown in Figure 10. The streamline scene shows how the injected water (red) interacts with the bulk flow of water (blue). It is apparent that without injection (Figure 10a), the bulk flow travels smoothly over the plate with only minor disturbance, consistent with the relatively high skin-friction distribution in Figure 9a. In comparison to the non-injection

case, the cases with injection demonstrate that there is a modification to the near-wall flow momentum. At U_{Inj}/U_b = 1.5, the jet flow induces flow separation and recirculation close to the wall, whilst the freestream flow remains relatively close to the wall. This reduces the velocity gradient at the wall and produces the lower skin friction seen in Figure 9c and explaining the peak drag reduction in Figure 7. Increasing the injection velocity further (U_{Inj}/U_b = 2.0–3.0; Figure 10d–e), the separation and recirculation region expands, and the bulk freestream penetrates deeper into the recirculation zone, leading to an increase in skin friction.

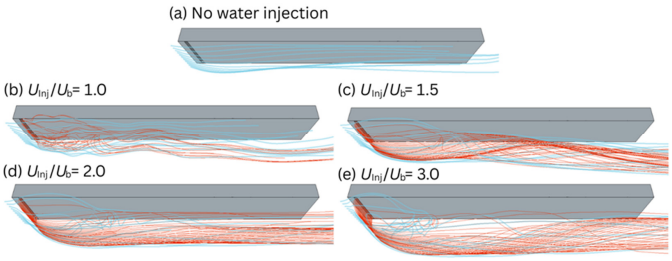

Figure 10. Streamlines of bulk flow (light blue) and injected flow (red): (**a**) no water injection, (**b**) U_{inj}/U_b = 1.0, (**c**) U_{inj}/U_b = 1.5, (**d**) U_{inj}/U_b = 2.0 and (**e**) U_{inj}/U_b = 3.0.

Figure 11 presents the streamwise variation in local drag reduction, DR(z), along the plate for different injection velocity ratios. For all cases, the profiles show that the effect of injection is highly non-uniform, with alternating regions of positive and negative drag reduction reflecting local changes in wall shear stress downstream of the slot. At U_{Inj}/U_b = 1.0 (Figure 11a), the distribution is strongly oscillatory, with significant peaks and troughs indicating strong sensitivity of the boundary layer to the injected momentum. Increasing the ratio to U_{Inj}/U_b = 1.5 (Figure 11b), which was identified as the optimum drag reduction (see Figure 7), yields the most favourable profile: after an initial negative pocket near the slot exit, the curve exhibits a broad positive region and gradually decays toward neutral values at the trailing edge. At U_{Inj}/U_b = 2.0 (Figure 11c), the negative dip immediately downstream of the slot deepens and extends further, and although a positive peak remains, the overall trend converges to smaller gains relative to the U_{Inj}/U_b = 1.5 case. For the highest ratio, U_{Inj}/U_b = 3.0 (Figure 11d), the profile is dominated by pronounced oscillations with extended negative zones, showing that excessive injection increases near-wall shear instead of reducing it. These distributions confirm that while moderate injection produces sustained drag reduction across most of the plate, higher ratios destabilise the boundary-layer development, leading to local drag penalties despite isolated regions of reduction.

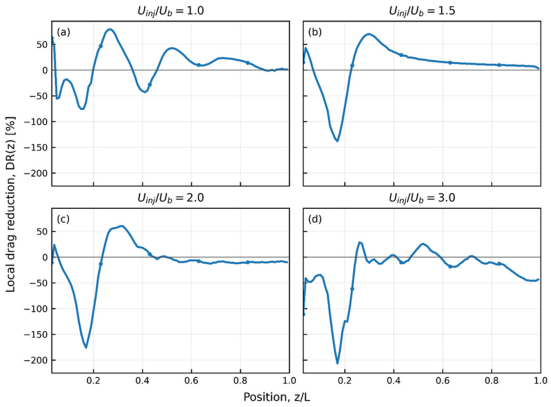

Figure 11. Streamwise distribution of local drag reduction, DR(z), along the plate surface for different injection velocity ratios. Results are shown for (**a**) U_{Inj}/U_b = 1.0, (**b**) U_{Inj}/U_b = 1.5, (**c**) U_{Inj}/U_b = 2.0,

and (**d**) U_{Inj}/U_b = 3.0. The horizontal axis is normalised by the plate length (z/L), with z/L = 0 at the slot exit and z/L = 1 at the trailing edge. Positive values of DR(z) indicate local skin-friction reduction relative to the baseline non-injection case.

5. Effect of Plate Orientation

At the highest Reynolds number tested (8.42×10^6) and with an injection velocity ratio, U_{Inj}/U_b = 1.33, the plate orientation was varied relative to the freestream direction (roll angle). The angles considered were 0 ° (flat plate), 15°, 30°, 45°, 60°, 75°, and 90° (vertical plate). This analysis aimed to evaluate the applicability of water injection for drag reduction on inclined or sidewall surfaces representative of ship hull geometries. The results are summarised in Figure 12. with the corresponding numerical values tabulated in Table A6 in Appendix B.

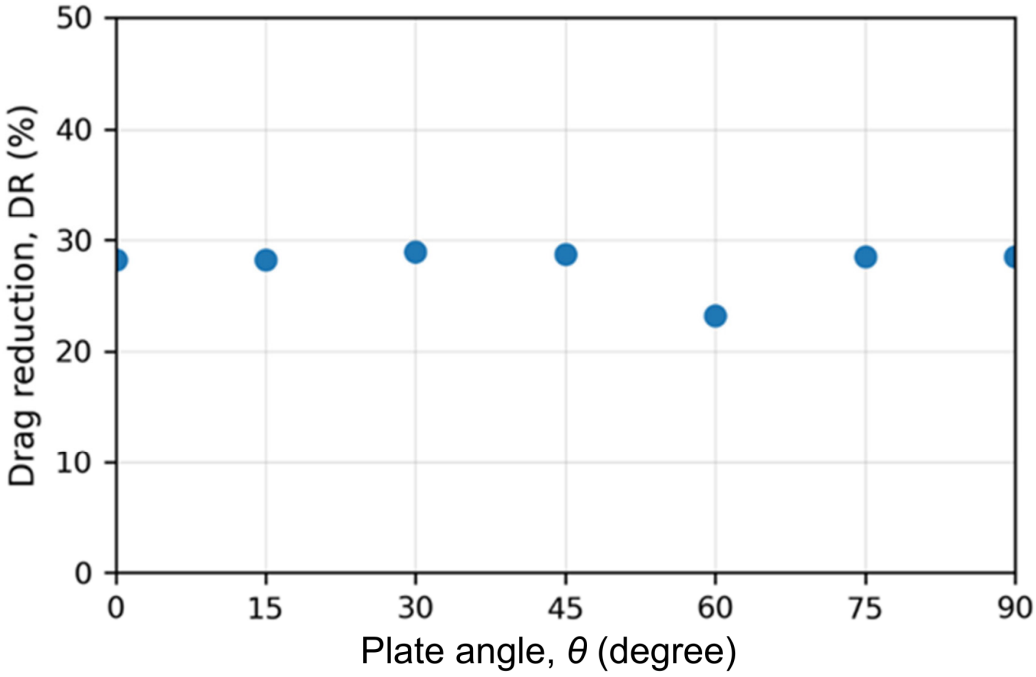

Figure 12. Effect of plate orientation on drag reduction at $Re_L = 8.42 \times 10^6$ and U_{Inj}/U_b =1.33.

Figure 12 shows that drag reduction remains stable across orientations, with values consistently between 28% and 30%. A minor dip occurs at 60°, which may reflect numerical or domain-related effects at steeper inclinations. Overall, the results indicate that the water-injection strategy is robust across a wide range of roll angles, supporting its potential application to inclined hull surfaces. To investigate the underlying mechanisms, contours of the pressure coefficient (C_P) and the skin-friction coefficient (C_f) at selected orientations are presented in Figure 13.

As the plate is rotated in the xy plane from 0° to 90°, while remaining parallel to the flow direction, the surface pressure distribution in Figure 13 (left) changes markedly. At 0°, the pressure field is nearly uniform, but with increasing rotation, distinct high- and low-pressure regions appear on opposite sides of the plate, with the strongest contrast at 90°. This variation partly reflects the effect of gravity acting in $-$y direction, introduces a hydrostatic pressure bias when the plate is rolled.

In contrast, the skin-friction patterns in Figure 13 (centre) remain broadly similar across orientations. As seen previously in Figure 9, the no-injection cases exhibit nearly symmetric distributions. In contrast, the injection cases exhibit asymmetric patterns with alternating regions of high and low skin friction, associated with displaced low-velocity

zones near the slot. At 60° (Figure 13c, centre), the skin-friction distribution appears more symmetric, consistent with the modest dip in drag reduction observed in Figure 12. The deviation is attributed to side-wall confinement from the limited tank width, a minor effect that does not change the overall conclusion. Additional analysis of the turbulent kinetic energy (TKE) distribution (Figure 13c, right) was conducted to assess the effect of roll angle. The results showed that TKE remained nearly unchanged across all orientations, indicating that plate rotation has little influence on near-wall turbulence intensity.

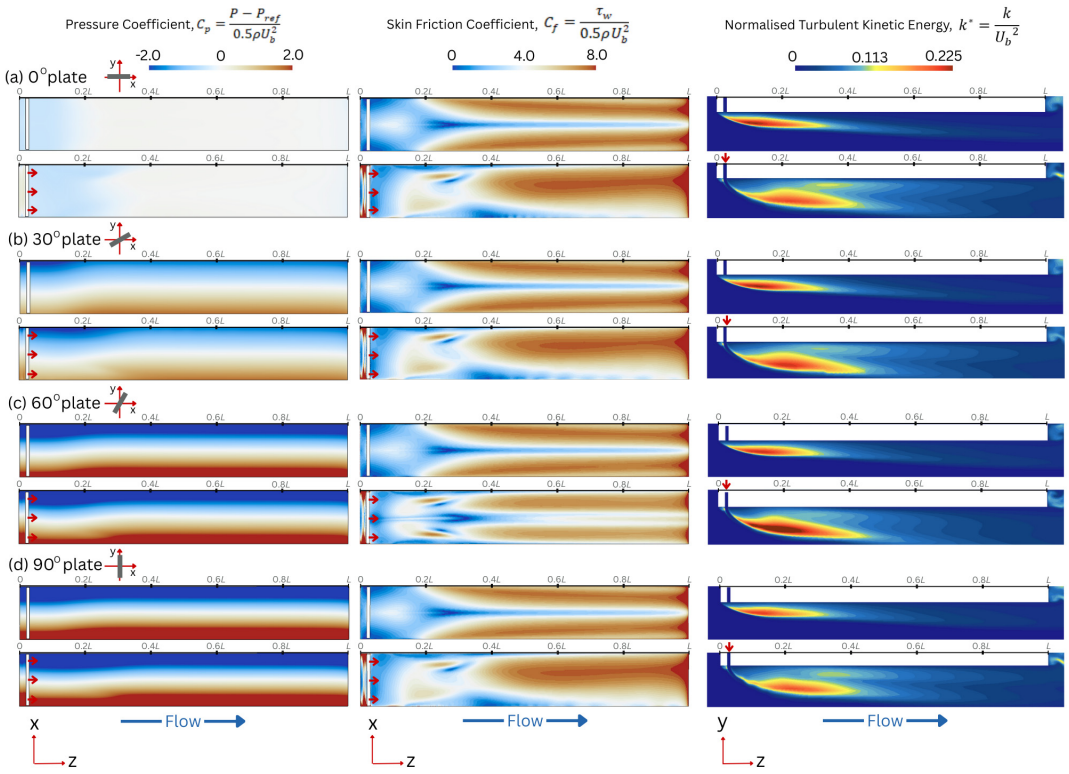

Figure 13. Contours of (**left**) pressure coefficient, C_p, (**centre**) skin friction coefficient, C_f, and (**right**) normalised turbulent kinetic energy, k/U_b^2, at selected plate orientations: (**a**) 0° (flat plate), (**b**) 30°, (**c**) 60° and (**d**) 90° (vertical plate). Simulations correspond to the highest Reynolds number tested (8.42×10^6) and with an injection velocity ratio, $U_{Inj}/U_b = 1.33$. In each subfigure, the top panel shows the case without injection, and the bottom panel shows the case with injection.

Overall, these results show that despite substantial changes in pressure with plate orientation, drag reduction remains nearly constant. This confirms that water injection reduces drag primarily through its influence on skin friction, which is largely insensitive to orientation. Unlike air injection, where performance is strongly affected by pressure distribution, water injection provides robust drag-reduction benefits across all plate angles. Nevertheless, further investigation, ideally through towing tank experiments, is recommended to fully characterise the influence of plate angle under realistic flow conditions.

The present model is simplified and does not reproduce the streamlined curvature of a full ship hull. It isolates local water-injection physics on a planar wall, providing a controlled basis for comparison and a useful step towards future experimental and full-scale validation.

6. Conclusions

This study presented a systematic numerical investigation into water-injection drag reduction on a rectangular flat-plate model, utilising validated RANS simulations and rigorous verification. The findings strongly support the viability of water injection as

a robust and scalable strategy for maritime decarbonisation. Water injection achieved significant drag reduction, with the maximum observed reduction of up to 38.8% delivered at an optimal injection velocity ratio of U_{Inj}/U_b = 1.5. The technology is most effective when the injection angle is between 60° and 90°. Furthermore, the injection velocity ratio (U_{Inj}/U_b) proved to be the more reliable non-dimensional scaling parameter, maintaining drag reduction levels of 30–40% across a wide range of Reynolds numbers. Analysis of the flow fields confirmed that the primary mechanism for drag reduction is the modification of skin friction through the stable formation of a low-velocity recirculation layer near the wall. Crucially, a key finding is the insensitivity of drag reduction to plate orientation (roll angle), confirming that the technology primarily impacts skin friction and is not dependent on pressure distribution, which makes it a more versatile alternative for complex hull geometries and side-wall lubrication than air lubrication. Future work should focus on experimental validation at larger scales, optimisation of slot geometry and injection layout, and the integration into realistic ship hull designs to fully assess the full-scale energy-saving potential.

Author Contributions: Conceptualization, D.H., E.B.-D. and A.S. (Andrew Spiteri); Methodology, D.H. and A.S. (Andrew Spiteri); Software, D.H.; Validation, D.H. and A.M.P.; Formal analysis, D.H. and A.M.P.; Investigation, D.H. and A.M.P.; Resources, D.H., E.B.-D. and J.W.; Data curation, D.H.; Writing—original draft, D.H. and A.M.P.; Writing—review & editing, D.H., A.M.P., E.B.-D., A.S. (Andrew Spiteri), A.S. (Ava Shahrokhi), A.R., R.A., N.T. and J.W.; Visualization, D.H.; Supervision, E.B.-D., A.S. (Ava Shahrokhi) and J.W.; Project administration, E.B.-D., A.S. (Ava Shahrokhi), A.R., R.A., N.T. and J.W.; Funding acquisition, E.B.-D., A.R., R.A., N.T. and J.W. All authors have read and agreed to the published version of the manuscript.

Funding: This research was supported by the UK National Clean Maritime Research Hub (CMRH-004, Ref: EP/Y024605/1), funded by the Engineering and Physical Sciences Research Council (EPSRC) and the Department for Transport, through the project "H2O COLORADO (Water Injected Boundary Layer Modification for Drag Reduction)".

Data Availability Statement: The data that supports the findings of this study are available from the corresponding author upon reasonable request.

Acknowledgments: The authors would like to thank the industrial partners involved, Laskaridis Maritime and Armada Technologies, for their contribution to the project and their valuable feedback on this publication and the project report.

Conflicts of Interest: Alex Routledge and Roger Armson were employed by Armada Technologies. Nikolaos Tsoulakos was employed by Laskaridis Shipping Co., Ltd. The remaining authors declare that the research was conducted in the absence of any commercial or financial relationships that could be construed as a potential conflict of interest.

Abbreviations

The following abbreviations are used in this manuscript:

AMG	Algebraic Multigrid
CFD	Computational Fluid Dynamics
DR	Drag Reduction
ITTC	International Towing Tank Conference
JBC	Japan Bulk Carrier
LJMU	Liverpool John Moores University
RANS	Reynolds-Averaged Navier–Stokes
Re	Reynolds number
SST	Shear Stress Transport
VOF	Volume of Fluid

Symbols

The following symbols are used in this manuscript:

A_{Inj}	Cross-sectional area of the injection slot
B_{Inj}	Width of the injection slot
B_{Tank}	Width of the tank
B_{WL}	Width of the flat plate
C_f	Skin frictional coefficient
C_P	Pressure coefficient
ε_F	Relative uncertainty
F_D	Skin frictional drag force with injection
F_{D0}	Skin frictional drag force without injection
F_{Fit}	Best fit curve
K	Turbulent kinetic energy
L	Length of the flat plate
L_{inj}	Length of the injection slot
L_{Tank}	Length of the tank
P	Pressure
P_{ref}	Reference pressure
Q_{Inj}	Volumetric injection rate
Q_{Inj}/Q_w	Injection flow rate ratio
Q_w	Volumetric flow within the boundary layer
Re_L	Reynolds number on the plate
T	Height of the flat plate
T_{Tank}	Height of the tank
U_b	Bulk velocity/Freestream velocity
U_{Inj}	Injection velocity
U_{Inj}/U_b	Injection velocity ratio
y^+	Non-dimensional wall distance
Δt	Time step size
Δx	Base cell size
ν	Kinematic viscosity
ρ	Density of water
τ_w	Wall shear stress

Appendix A. Dimensional Analysis

To enhance repeatability, the Buckingham Pi theorem [29], a widely used tool in dimensional analysis, identifies relevant dimensionless groups with the following steps:

Appendix A.1. List Down All Variables and Choose Repeating Variables

In the analysis of water-lubrication, the variables involve only three fundamental dimensions: mass (M), length (L), and time (T), which are used to identify the skin frictional drag force, F_D. The variables and their dimensions are detailed in Table A1.

Table A1. Dependent and independent variables with dimensions.

Variables	Dimensions
Dependent:	
Skin friction drag force, F_D	ML/T^2
Independent:	
Bulk Velocity, U	[L/T]
Density of water, ρ	$[M/L^3]$
Knematic viscosity, v	$[L^2/T]$
Injection velocity, U_{inj}	[L/T]
Injection area, A_{inj}	$[L^2]$
Length of plate, L	[L]
Width of plate, B_{WL}	[L]

The 8 variables consist of three independent dimensions: mass (M), length (L), and time (T), necessitating the formation of 5 dimensionless groups. The chosen repeating variables are density of water, ρ, bulk velocity, U_b, and plate length, L.

Appendix A.2. Dimensionless Groups

Aside from the scaling variables, the remaining variables in Table A1 are made dimensionless using the repeated variables. By inspection, numerical multipliers have been applied to correlate with established dimensionless groups commonly used in the fluid field, as given in the following Table A2.

Table A2. Dimensionless groups.

Derived From	Dimensionless Groups	Variables	Formula
		Dependent:	
F_D	Π_1	Skin friction coefficient	$C_f = F_D/0.5\rho A U^2$
		Independent:	
v	Π_2	Reynolds number	$Re_L = U_b L/\nu$
U_b	Π_3	Injection velocity ratio	$U_r = U_{inj}/U_b$
A	Π_4	Injection area ratio	$A_r = A_{inj}/A$
B_{WL}	Π_5	Plate aspect ratio	$AR = L/B_{WL}$

For this analysis, the plate geometry (L and B) and injection area (A_{Inj}) have remained constant. Hence the dimensionless groups Π_4 (injection area ratio) and Π_5 (aspect ratio) remain unchanged.

By combining the remaining independent groups Π_2 (Reynolds number), Π_3 (injection velocity ratio), and Π_5 (aspect ratio), the injection flow-rate ratio, α, can be derived. This parameter is defined as the ratio of the injection flow rate, Q_{Inj} to the wall flow rate within the boundary layer, Q_w, following the formulation by [30]. Substituting $Q_{Inj} = U_{Inj}A_{Inj}$ and $Q_w = 0.293L^{0.8}\nu^{0.2}U^{0.2}B_{WL}$, and taking the plate wetted area as $A = L \times B_{WL}$ gives

$$\alpha = \frac{Q_{Inj}}{Q_w} = \frac{{Re_L}^{0.2}}{0.293} U_r AR \quad \text{(A1)}$$

where $Re_L = U_b L/\nu$ is the Reynolds number, $U_r = U_{Inj}/U_b$ is the injection velocity ratio, and $AR = A_{Inj}/(LB_{WL})$. The injection slot is neglected in the definition of the wetted area because its contribution is negligible: the slot area (0.039 m^2) is less than 1% of the total plate area (4.02 m^2).

Appendix B. Tabulated Results

This appendix presents the numerical values underlying the graphs shown in the Section 4. For completeness, the results are tabulated to include drag forces and percentage drag reductions under various test conditions, namely: injection angle, injection velocity ratio, injection flow rate ratio, Reynolds number, and plate orientation. These tables provide a direct reference for the quantitative values discussed in the main text.

Table A3. Drag forces and percentage drag reduction for different injection angles at U_b = 1.0 m/s ($Re_L = 5.61 \times 10^6$) and U_{Inj}/U_b = 2.0. Each drag reduction value is referenced to its corresponding no-injection case with the slot present.

Injection Angle, θ [º]	No Injection Drag Force, F_{D0} [N]	With Injection Drag Force, F_D [N]	Drag Reduction, DR [%]
15	3.683	132.213	−3489.8%
30	3.549	27.863	−685.1%
45	3.560	7.761	−118.0%
60	3.36	3.150	10.9%
75	3.547	2.978	16.1%
90	3.670	2.917	20.5%

Table A4. Drag forces and percentage drag reduction for varying injection velocity ratios, U_{Inj}/U_b at U_b = 1.0 m/s ($Re_L = 5.61 \times 10^6$) and injection angle, θ = 90.

Injection Velocity Ratio, U_{inj}/U_b	Injection Flow Rate Ratio, Q_{inj}/Q_w	No Injection Drag Force, F_{D0} [N]	With Injection Drag Force, F_D [N]	Drag Reduction, DR [%]
0.1	0.07		3.505	4.5%
0.2	0.15		3.432	6.5%
0.3	0.22		3.357	8.5%
0.4	0.30		3.260	11.2%
0.5	0.37		3.156	14.0%
1.0	0.74		2.762	24.7%
1.2	0.89		2.679	27.0%
1.4	1.04	3.67	2.662	27.5%
1.45	1.07		2.312	37.0%
1.5	1.11		2.245	38.8%
1.6	1.19		2.651	27.8%
1.8	1.33		2.749	25.1%
2	1.48		2.917	20.5%
2.5	1.85		3.231	12.0%
3	2.22		3.433	6.5%

Table A5. Drag forces and percentage drag reduction for varying injection ratios on drag reduction at fixed bulk velocity of U_b = 1 m/s and U_b = 1.5 m/s.

Bulk Velocity, U_b	Injection Velocity Ratio, U_{inj}/U_b	Injection Flow Rate Ratio, Q_{inj}/Q_w	No Injection Drag Force, F_{D0} [N]	With Injection Drag Force, F_D [N]	Drag Reduction, DR [%]
1.0 m/s	0.1	0.07	3.67	3.505	4.5%
	0.2	0.15		3.432	6.5%
	0.3	0.22		3.357	8.5%
	0.4	0.30		3.260	11.2%
	0.5	0.37		3.156	14.0%
	1.0	0.74		2.762	24.7%
	1.2	0.89		2.679	27.0%
	1.4	1.04		2.662	27.5%
	1.45	1.07		2.312	37.0%
	1.5	1.11		2.245	38.8%
	1.6	1.19		2.651	27.8%
	1.8	1.33		2.749	25.1%
	2	1.48		2.917	20.5%
	2.5	1.85		3.231	12.0%
	3	2.22		3.433	6.5%
1.5 m/s	0.124	0.1	7.822	7.704	2%
	0.373	0.3		7.478	4%
	0.622	0.5		6.739	14%
	0.871	0.7		5.983	24%
	1.120	0.9		5.835	25%
	1.369	1.1		5.864	25%
	1.618	1.3		5.931	24%
	1.867	1.5		6.298	19%

Table A6. Drag forces and percentage drag reduction at varying Reynolds number, Re_L, at a fixed non-dimensional injection parameter: injection velocity ratio, U_{Inj}/U_b = 1.5, and injection flow rate ratio, Q_{Inj}/Q_w = 1.1.

Constant Non-Dimensional Unit	Reynolds Number, Re_L	No Injection Drag Force, F_{D0} [N]	With Injection Drag Force, F_D [N]	Drag Reduction, DR [%]
U_{inj}/U_b = 1.5	1.68×10^6	0.446	0.307	31.2%
	3.37×10^6	1.465	0.893	39.1%
	4.49×10^6	2.455	1.488	39.4%
	5.61×10^6	3.670	2.245	38.8%
	6.73×10^6	5.198	3.139	39.6%
Q_{inj}/Q_w = 1.1	1.68×10^6	0.446	0.288	35.4%
	3.37×10^6	1.465	0.858	41.4%
	4.49×10^6	2.455	1.765	28.1%
	5.61×10^6	3.670	2.234	39.1%
	6.73×10^6	5.198	3.508	32.5%
	8.42×10^6	7.822	5.864	25.0%

Table A7. Drag forces and percentage drag reduction for different plate orientations at the highest Reynolds number tested (8.42×10^6) and with injection velocity ratio, U_{inj}/U_b = 1.33.

Plate Orientation	No Injection Drag Force, F_{D0} [N]	With Injection Drag Force, F_D [N]	Drag Reduction, DR [%]
0	8.141	5.842	28%
15	8.129	5.835	28%
30	8.146	5.787	29%
45	8.144	5.802	29%
60	8.148	6.256	23%
75	8.135	5.814	29%
90	8.105	5.795	28%

References

1. García-Mayoral, R.; Jiménez, J. Drag reduction by riblets. *Philos. Trans. R. Soc. A Math. Phys. Eng. Sci.* **2011**, *369*, 1412–1427. [CrossRef] [PubMed]
2. Bogdevich, V.; Evseev, A.; Malyuga, A.; Migirenko, G. Gas-saturation effect on near-wall turbulence characteristics. In Proceedings of the 2nd International BHRA Fluid Drag Reduction Conference, Cambridge, UK, 31 August–2 September 1977.
3. Giernalczyk, M.; Kaminski, P. Assessment of the propulsion system operation of the ships equipped with the air lubrication system. *Sensors* **2021**, *21*, 1357. [CrossRef] [PubMed]
4. Madavan, N.K.; Deutsch, S.; Merkle, C.L. Measurements of local skin friction in a microbubble-modified turbulent boundary layer. *J. Fluid Mech.* **1985**, *156*, 237–256. [CrossRef]
5. Barros, D.; Borée, J.; Noack, B.R.; Spohn, A.; Ruiz, T. Bluff body drag manipulation using pulsed jets and Coanda effect. *J. Fluid Mech.* **2016**, *805*, 422–459. [CrossRef]
6. Shereena, S.; Vengadesan, S.; Idichandy, V.; Bhattacharyya, S. CFD study of drag reduction in axisymmetric underwater vehicles using air jets. *Eng. Appl. Comput. Fluid Mech.* **2013**, *7*, 193–209. [CrossRef]
7. Suárez, P.; Alcántara-Ávila, F.; Miró, A.; Rabault, J.; Font, B.; Lehmkuhl, O.; Vinuesa, R. Active Flow Control for Drag Reduction Through Multi-agent Reinforcement Learning on a Turbulent Cylinder at R_eD = 3900. *Flow Turbul. Combust.* **2025**, *115*, 3–27. [CrossRef] [PubMed]
8. Beloki Perurena, J.; Asma, C.O.; Theunissen, R.; Chazot, O. Experimental investigation of liquid jet injection into Mach 6 hypersonic crossflow. *Exp. Fluids* **2009**, *46*, 403–417. [CrossRef]
9. Fedorova, N.N.; Goldfeld, M.A. Influence of Jet-to-Freestream Momentum Ratio and Gas Molecular Weight on Mixing at the Injection of Jets into a Supersonic Crossflow. *Tech. Phys. Lett.* **2021**, *47*, 50–55. [CrossRef]
10. Sonmez, A.U.; Vijayan, S.N. Numerical Analysis of Frictional Drag Reduction of Watercraft Using Water Lubrication Technique. In *Engineering and Technology Quarterly Reviews*; Asian Institute of Research: Makassar, Indonesia, 2022; Volume 5, pp. 18–29.

11. Kou, J.; Lou, Q.; Gu, Y.; Zhang, J.; Mou, C.; Yu, J.; Ding, Y.; Xu, C. Analysis of Surface Drag Reduction Characteristics of Non-Smooth Jet Coupled Structures. *Lubricants* **2024**, *12*, 334. [CrossRef]
12. Rotte, G.; Zverkhovskyi, O.; Kerkvliet, M.; van Terwisga, T. On the physical mechanisms for the numerical modelling of flows around air lubricated ships. In Proceedings of the International Conference on Hydrodynamics (ICMF), Egmond aan Zee, The Netherlands, 18–23 September 2016.
13. Shah, Y.; Yarusevych, S. Streamwise evolution of drag reduced turbulent boundary layer with polymer solutions. *Phys. Fluids* **2020**, *32*, 065108. [CrossRef]
14. Xie, L.; Shi, P.-F.; Li, H.-R.; Liu, H.; Hu, H.-B. Drag reduction by natural yam mucilage in turbulent flows. *Phys. Fluids* **2024**, *36*, 013114. [CrossRef]
15. Liu, H.; Hu, H.-B.; Xie, L.; Shi, P.-F.; Wen, J.; Li, Y.-K.; Tang, S.-L. The drag reduction performance by slowly releasing polymer solution through porous media. *Phys. Fluids* **2025**, *37*, 085166. [CrossRef]
16. Spiteri, A. An Investigation of the Hydrodynamics of Air Lubrication Systems and the Development of a Scaling Technique for Different Designs and Operational Conditions Using CFD. Ph.D. Thesis, Liverpool John Moores University, Liverpool, UK, 2024.
17. Cucinotta, F.; Guglielmino, E.; Sfravara, F.; Strasser, C. Numerical and experimental investigation of a planing Air Cavity Ship and its air layer evolution. *Ocean. Eng.* **2018**, *152*, 130–144. [CrossRef]
18. Siemens. *Siemens STAR CCM+ User Guide*; Siemens: Munich, Germany, 2019.
19. Abidin, N.Z.; Grondin, F.; Muller, P.; Sigrist, J.-F. Comprehensive Numerical Hydrodynamic Analysis of Submarine in a Straight Course Simulation Using Wall-Resolved RANS Models. *arXiv* **2025**, arXiv:2510.04911. [CrossRef]
20. Pena, B.; Huang, L. A review on the turbulence modelling strategy for ship hydrodynamic simulations. *Ocean. Eng.* **2021**, *241*, 110082. [CrossRef]
21. LJMU, A. Prospero Specifications. Available online: https://prospero-docs.readthedocs.io/en/latest/specifications.html (accessed on 15 September 2025).
22. Siemens. *Prism Layer Meshing for Effective Boundary Layer Capturing Agenda*; Online Presentation; Siemens: Munich, Germany, 2019.
23. Maki, K.; Zhao, F.; Horn, P.; Banks, J.; Martio, J.; Starke, B.; Zaghi, S.; Villa, D.; Vitola, M.; Yoon, H.S.; et al. *Uncertainty Analysis in CFD Verification and Validation Methodology and Procedures*; Procedure 7.5-03-01-01, Rev. 05; ITTC: Zürich, Switzerland, 2024.
24. Eça, L.; Hoekstra, M. A procedure for the estimation of the numerical uncertainty of CFD calculations based on grid refinement studies. *J. Comput. Phys.* **2014**, *262*, 104–130. [CrossRef]
25. Malki, K.; Zhao, F.; Horn, P.; Banks, J.; Martio, J.; Starke, B.; Zaghi, S.; Villa, D.; Vitola, M.; Yoon, H.S.; et al. *Practical Guidelines for Ship CFD Applications*; Procedure 7.5-03-02-03, Rev. 02; ITTC: Zürich, Switzerland, 2011.
26. Schlichting, H.; Gersten, K. *Boundary-Layer Theory*; Springer: Berlin/Heidelberg, Germany, 2016.
27. Schlichting, H. *Boundary-Layer Theory*; McGraw-Hill: Columbus, OH, USA, 1968.
28. Schultz, M.; Flack, K. The rough-wall turbulent boundary layer from the hydraulically smooth to the fully rough regime. *J. Fluid Mech.* **2007**, *580*, 381–405. [CrossRef]
29. Bertrand, J. Sur l'homogénéité dans les formules de physique. *Cah. Rech. L'academie Sci.* **1878**, *86*, 916–920.
30. Sayyaadi, H.; Nematollahi, M. Determination of optimum injection flow rate to achieve maximum micro bubble drag reduction in ships; an experimental approach. *Sci. Iran.* **2013**, *20*, 535–541.